NASA/TP-2015-218698

GCR Simulator Reference Field and a Spectral Approach for Laboratory Simulation

Tony C. Slaba, Steve R. Blattnig, and John W. Norbury
Langley Research Center, Hampton, Virginia

Adam Rusek and Chiara La Tessa
Brookhaven National Laboratory, Upton, New York

Steven A. Walker,
Old Dominion University Research Foundation, Norfolk, Virginia

March 2015

NASA STI Program . . . in Profile

Since its founding, NASA has been dedicated to the advancement of aeronautics and space science. The NASA scientific and technical information (STI) program plays a key part in helping NASA maintain this important role.

The NASA STI program operates under the auspices of the Agency Chief Information Officer. It collects, organizes, provides for archiving, and disseminates NASA's STI. The NASA STI program provides access to the NTRS Registered and its public interface, the NASA Technical Reports Server, thus providing one of the largest collections of aeronautical and space science STI in the world. Results are published in both non-NASA channels and by NASA in the NASA STI Report Series, which includes the following report types:

- TECHNICAL PUBLICATION. Reports of completed research or a major significant phase of research that present the results of NASA Programs and include extensive data or theoretical analysis. Includes compilations of significant scientific and technical data and information deemed to be of continuing reference value. NASA counter-part of peer-reviewed formal professional papers but has less stringent limitations on manuscript length and extent of graphic presentations.

- TECHNICAL MEMORANDUM. Scientific and technical findings that are preliminary or of specialized interest, e.g., quick release reports, working papers, and bibliographies that contain minimal annotation. Does not contain extensive analysis.

- CONTRACTOR REPORT. Scientific and technical findings by NASA-sponsored contractors and grantees.

- CONFERENCE PUBLICATION. Collected papers from scientific and technical conferences, symposia, seminars, or other meetings sponsored or co-sponsored by NASA.

- SPECIAL PUBLICATION. Scientific, technical, or historical information from NASA programs, projects, and missions, often concerned with subjects having substantial public interest.

- TECHNICAL TRANSLATION. English-language translations of foreign scientific and technical material pertinent to NASA's mission.

Specialized services also include organizing and publishing research results, distributing specialized research announcements and feeds, providing information desk and personal search support, and enabling data exchange services.

For more information about the NASA STI program, see the following:

- Access the NASA STI program home page at http://www.sti.nasa.gov

- E-mail your question to help@sti.nasa.gov

- Phone the NASA STI Information Desk at 757-864-9658

- Write to:
  NASA STI Information Desk
  Mail Stop 148
  NASA Langley Research Center
  Hampton, VA 23681-2199

NASA/TP-2015-218698

GCR Simulator Reference Field and a Spectral Approach for Laboratory Simulation

Tony C. Slaba, Steve R. Blattnig, and John W. Norbury
Langley Research Center, Hampton, Virginia

Adam Rusek and Chiara La Tessa
Brookhaven National Laboratory, Upton, New York

Steven A. Walker,
Old Dominion University Research Foundation, Norfolk, Virginia

National Aeronautics and
Space Administration

Langley Research Center
Hampton, Virginia 23681-2199

March 2015

Available from:

NASA STI Program / Mail Stop 148
NASA Langley Research Center
Hampton, VA 23681-2199
Fax: 757-864-6500

Contents

Figures

Tables

Abstract

The galactic cosmic ray (GCR) simulator at the NASA Space Radiation Laboratory (NSRL) is intended to deliver the broad spectrum of particles and energies encountered in deep space to biological targets in a controlled laboratory setting. In this work, certain aspects of simulating the GCR environment in the laboratory are discussed. Reference field specification and beam selection strategies at NSRL are the main focus, but the analysis presented herein may be modified for other facilities. First, comparisons are made between direct simulation of the external, free space GCR field and simulation of the induced tissue field behind shielding. It is found that upper energy constraints at NSRL limit the ability to simulate the external, free space field directly (i.e. shielding placed in the beam line in front of a biological target and exposed to a free space spectrum). Second, variation in the induced tissue field associated with shielding configuration and solar activity is addressed. It is found that the observed variation is likely within the uncertainty associated with representing any GCR reference field with discrete ion beams in the laboratory, given current facility constraints. A single reference field for deep space missions is subsequently identified. Third, an approach for selecting beams at NSRL to simulate the designated reference field is presented. Drawbacks of the proposed methodology are discussed and weighed against alternative simulation strategies. The neutron component and track structure characteristics of the simulated field are discussed in this context.

Introduction

Exposure to galactic cosmic rays (GCR) on long duration missions presents a serious health risk to astronauts [NCRP 2006, NRC 2006] with large uncertainties associated with the biological response [NCRP 2012, Cucinotta et al. 2013]. In order to reduce these uncertainties, radiobiology experiments are performed to elucidate the basic mechanisms through which cancer and other endpoints are initiated by space radiation exposure. An important goal, and complicating feature, of the experiments is to collectively span the broad range of energies, particle species, and low dose rates (~mSv/day) characteristic of the space radiation environment. Individual studies typically consider a small number of particle species or energies. This approach is guided in part by the desire to gain a basic understanding of the mechanisms through which radiation interacts with biological targets but also by limitations with particle accelerator facilities and cost.

The NASA Space Radiation Laboratory (NSRL) at Brookhaven National Laboratory (BNL) has been supporting radiobiology experiments for over a decade, and additional facilities are being built elsewhere with overlapping research interests [Durante et al. 2007], such as the Facility for Anti-proton and Ion Research (FAIR) at GSI. The accelerator at NSRL has generally matured to a point where simulating a broad spectrum of particle types and energies encountered in deep space within a single experiment is feasible from a technology and cost perspective. The main purpose of such an experiment, referred to herein as a GCR simulation, would be to deliver the radiation environment encountered by astronauts in deep space to biological targets in a controlled laboratory setting. These experiments may be used to study a variety of topics associated with mixed radiation fields, such as countermeasure development and testing, as well as dose rate, cardiovascular, and central nervous system (CNS) effects.

Many of the details associated with designing a GCR simulator will depend on the biological question and endpoint being studied. However, some aspects of the simulator can be standardized across experiments to enable subsequent cross comparisons and validation. The present work focuses on two aspects of GCR simulator design at NSRL that allow some level of standardization: reference field specification and a general beam selection strategy. The term reference field is used here to describe the space radiation environment being represented in the GCR simulator. The beam selection strategy described herein includes constraints that are specific to NSRL but could be easily modified for other facilities.

Two basic strategies for beam selection are discussed presently and are depicted in Figure 1. In one approach, the external, free space GCR spectrum is represented by discrete ion and energy beams and delivered onto a shielding material placed within the beam line, in front of the biological target. The shielding material is used to modulate the primary beams in a manner similar to vehicle or habitat shielding for a deep space mission. This approach is referred to throughout this paper as simulating the external GCR environment directly, or the external field approach. The key feature is that the accelerator facility provides the ions and energies necessary to accurately reproduce the unmodified, external, free space GCR spectrum. In the other approach, models are used to

characterize the induced radiation field found within a representative tissue of an astronaut behind shielding. The induced (or local) tissue field is then represented by discrete ion and energy beams and delivered directly onto the biological target. This approach is referred to throughout this paper as simulating the local tissue field, or the local field approach. Note that in either approach, a reference field is required to guide beam selection. In the external field approach, the reference field is a representative free space GCR spectrum (e.g. unmodified, free space solar minimum environment). In the local tissue field approach, the reference field is a representative shielded tissue spectrum found in space (e.g. average tissue flux behind vehicle shielding during solar minimum).

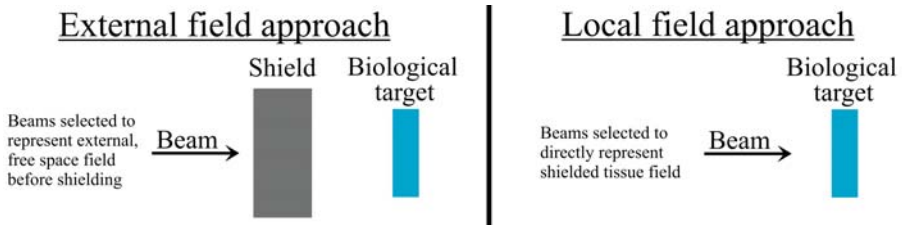

Figure 1. External and local tissue field approaches for selecting beams in the GCR simulator.

In this work, two aspects of simulating the GCR environment in the laboratory are studied: reference field specification and general beam selection strategy. First, a reference environment for the laboratory simulation is identified. This includes analysis and discussion related to the external, free space environment, the induced environment behind shielding and tissue, as well as the impacts of shielding and solar activity. Second, sensitivity analysis results are given to identify the ions and energies of greatest importance in the reference field for exposure quantities of interest. The impacts of accelerator facility constraints are also considered with an emphasis on lower energy limitations of the experimental design and upper energy limitations of the accelerator. Third, an approach for simulating the reference field at an accelerator facility is presented. The approach considers the hydrogen ($Z = 1$) and helium ($Z = 2$) energy spectra individually, and heavier ions are represented by considering the associated linear energy transfer (LET) spectrum from the reference environment. This hybrid approach allows the full reference environment to be approximately represented with relatively few discrete ion and energy beams. Other quantities such as dose equivalent and the track structure parameter spectrum [Cucinotta et al. 2013] are used to independently verify that certain characteristics of the reference field are maintained by the beam selection. Increasing the number of discrete ion and energy beams is shown to systematically improve the representation of the reference environment. Finally, drawbacks of the proposed methodology are discussed and weighed against drawbacks of alternative strategies. The neutron component and track structure characteristics of the proposed strategy are also discussed within this context.

Reference Environment

In this section, a reference environment is identified for the laboratory simulation. The first part examines whether the external field approach or local tissue field approach is more appropriate given accelerator constraints and other factors. It is found that NSRL energy constraints limit the ability to simulate the external, free space GCR field. Drawbacks of simulating the shielded tissue field are similarly discussed. Other strategies for experimentally delivering the GCR environment could also be considered (i.e. some combination of the above mentioned strategies), but are likely to impose added complexity requiring further analysis to ensure the field being delivered is fully understood.

The second part of this section examines variation of the induced radiation field as a function of tissue location within the body, shielding thickness, shielding material, and solar activity. This quantifies the expected variation in the physical description of the induced tissue field and is used to determine whether or not multiple reference environments need to be considered.

Simulating external and local tissue fields

As the external GCR environment passes through shielding and tissue, it is modified due to atomic and nuclear interactions, as shown in Figure 2. Primary particles are slowed and may suffer a nuclear collision in which a spectrum of secondary particles is produced. In Figure 2, it is clear that the ^{16}O and ^{56}Fe particle spectra are greatly attenuated even through minimal shielding (5 g/cm^2 aluminum) and average body thickness (30 g/cm^2 water) due to

atomic slowing down and nuclear attenuation. The ^{1}H and ^{4}He spectra are similarly attenuated at high energies behind shielding, but the low energy portion of the spectra are actually amplified, representing gains from secondary particle production. Also evident in the figure is the absence of a neutron component in free space but a significant flux of neutrons behind even minimal shielding.

Clearly, the induced field behind shielding differs substantially from the primary field and, in some cases, may actually present an increased risk to the astronaut [Slaba et al. 2013a]. The significant influence of intervening shielding material then requires consideration as to whether the external, unmodified GCR environment or the internal, induced tissue environment should be simulated in the experimental setup. Accelerator facility constraints heavily influence these considerations, as energies beyond current facility capabilities may be important. Secondary particles such as neutrons or pions may also be present in the tissue field but are difficult to provide directly in the beam line. It should again be noted that if one attempts to simulate the external GCR field, some thickness of shielding material or materials would need to be placed within the beam line, in front of the biological target, to allow atomic slowing down and nuclear processes to modify the primary particles in a manner similar to Figure 2.

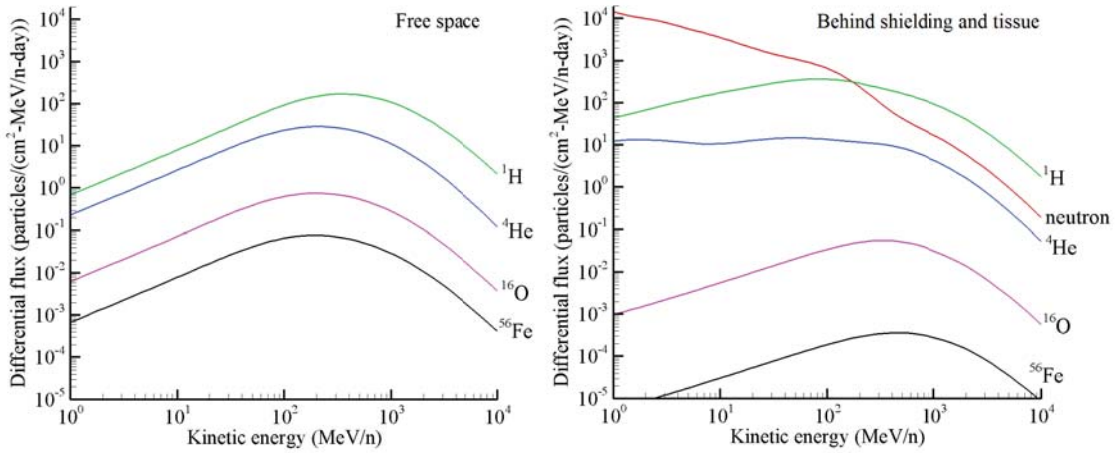

Figure 2. Comparison of selected GCR particle energy spectra in free space (left pane) and behind 5 g/cm^2 of aluminum and 30 g/cm^2 of water (right pane) during solar minimum. The Badhwar-O'Neill GCR model [O'Neill 2010] and HZETRN [Wilson et al. 1991, Slaba et al. 2010a,b] transport code were used.

In order to address the question of whether to simulate the external GCR environment or induced field behind shielding and tissue, sensitivity analyses are performed to identify which energies contribute most heavily to tissue exposure in each scenario. Such a study was recently completed [Slaba and Blattnig 2014a] to characterize the GCR energies impinging on shielding that contribute most significantly to effective dose behind shielding. A similar analysis is used here and extended to determine which energies are most important in both of the GCR simulator scenarios (i.e. simulating external field vs. simulating local tissue field). Results are shown in Figure 3 for various thicknesses of spherical aluminum shielding during solar minimum conditions. The left pane in the figure shows the cumulative fraction of effective dose as a function of the external, boundary energy impinging on the shield. The right pane shows the same quantity as a function of the local energy within the tissue. Effective dose has been computed as the weighted sum of tissue dose equivalent values determined in a detailed human phantom model. A more detailed description of the transport code, tissue weights, human phantom, and quality factor (for dose equivalent) is given in the following section. Results for solar maximum boundary conditions and other exposure quantities, such as individual tissue doses, were also computed and found to be qualitatively similar to those shown in Figure 3.

The results in the left pane of Figure 3 are relevant for the scenario in which the external field is simulated and shielding is placed in the beam line in front of the biological target (i.e. simulate external field directly, as in the left pane of Figure 1). In this case, it is found that boundary energies less than 1.5 GeV/n induce 35%-54% of the effective dose behind shielding. The energy value of 1.5 GeV/n was considered in previous sensitivity analyses [Slaba and Blattnig 2014a] and is being used here as a proxy for NSRL constraints which currently allow protons up to 2.5 GeV and heavier ions up to 1 GeV/n. The results in the right pane of Figure 3 are relevant for the scenario in which the internal tissue field is simulated (i.e. simulate shielded tissue field directly, as in the right pane of Figure 1). In this case, it is found that 83%-88% of the exposure is delivered by local energies less than 1.5 GeV/n. Clearly, the current NSRL constraints are less of a concern if the local field is simulated.

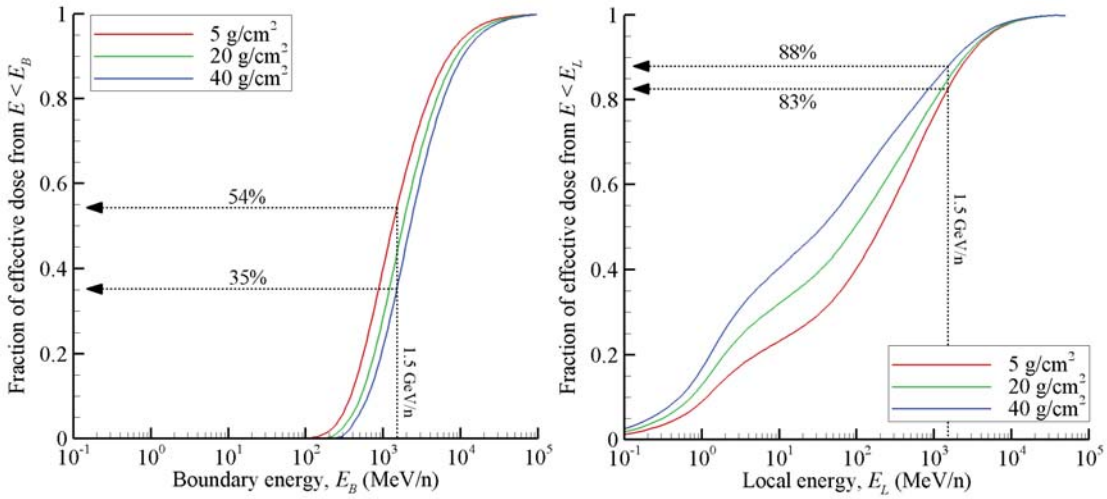

Figure 3. Fraction of effective dose as a function of the external, boundary energy impinging on the shield (left pane) and as a function of the local energy within the tissue (right pane). Results shown for solar minimum conditions and various thicknesses of spherical aluminum shielding. The energy of 1.5 GeV/n is identified with dashed lines in both plots.

Table 1. Fraction of effective dose delivered by energies below NSRL limitations (current and upgrade) behind spherical aluminum shielding thicknesses.

Energy cutoff description	Free space field			Local field		
	5 g/cm^2	20 g/cm^2	40 g/cm^2	5 g/cm^2	20 g/cm^2	40 g/cm^2
Protons up to 2.5 GeV and heavier ions up to 1.0 GeV/n	0.53	0.47	0.43	0.85	0.88	0.90
Protons up to 4 GeV and heavier ions up to 1.5 GeV/n	0.68	0.63	0.59	0.90	0.91	0.93

Instead of the proxy value of 1.5 GeV/n, the precise NSRL energy constraints were considered as well (see Table 1). One arrives at virtually the same conclusion that current facility energy limitations make it difficult to fully simulate the external GCR environment. If proposed facility upgrades are considered, which allow protons up to 4 GeV and heavier ions up to 1.5 GeV/n, the ability of simulating the free space field is improved, but still limited, compared to simulation of the local field directly.

It is interesting to discuss some of the trends observed in Figure 3 (and Table 1). In the left pane of the figure, it is seen that as shielding thickness increases, more substantial boundary energies are needed to deliver the same fraction of effective dose. To achieve 85% of the effective dose behind shielding – the approximate amount achieved by simulating the local field within current NSRL constraints – upper energy limits would need to be increased to 5 GeV/n – 8 GeV/n, depending on shielding. The right pane of Figure 3 shows that as shielding thickness increases, local energies greater than 1.5 GeV/n make less of a contribution to the exposure. The exposure is instead dominated by lower energy particles with high LET. Further, as the shielding thickness is increased, heavy ions ($Z > 2$) are more likely to be broken up by nuclear collisions, producing a radiation field dominated by nucleons and light ion ($Z \leq 2$) target fragments with energies well below 1.5 GeV/n [Cucinotta et al. 1996a, 1996b; Walker et al. 2013a; Norbury and Slaba 2014].

The right pane of Figure 3 establishes that current NSRL energy constraints are not restrictive if the induced tissue field behind shielding is simulated directly. A drawback of this approach is that secondary particles present in the induced tissue field, such as neutrons and the pion/electromagnetic (π/EM) cascade, cannot be directly provided within the NSRL beam line. It will be shown later that the neutron and π/EM components, combined, account for ~15% of the tissue dose or dose equivalent. It can be argued that even if these particles are fully neglected in the simulator design, the proposed strategy is still preferable to simulating the external, free space field where 46%-65% of the exposure profile is lost due to current NSRL energy constraints. Further discussion of the neutron and π/EM components is given later in this paper.

Based on these results and discussion, hereafter, it is assumed that the GCR simulator will be focused on directly reproducing the induced field found within tissue and behind shielding (as in the right pane of Figure 1). The next section examines variation of the induced radiation field as a function of tissue location within the body, shielding configuration, and solar activity. The motivation for this analysis is to determine whether or not multiple reference fields need to be considered for the simulator.

Variation in the induced tissue field: Shielding configuration and tissue location

The radiation field found within human tissue in space depends on the tissue location within the body, shielding configuration, and solar activity. Factors such as astronaut location and orientation within the vehicle contribute minimal variation for GCR environments and will not be considered [Wilson et al. 1993, Clowdsley et al. 2006]. The motivation for the analysis and discussion in this section is to determine if the variation in the induced tissue field either allows a single reference field or requires multiple reference fields to be defined for the GCR simulator. If the observed variation is within physics uncertainties [Wilson et al. 2005, Cucinotta et al. 2013, Slaba et al. 2013b] and the experimental design uncertainty associated with representing the reference field with comparatively few discrete mono-energetic ion beams, a single reference field is both sufficient and beneficial at this time. The benefit to having a single reference field is that multiple experiments utilizing the simulator will all be based on the same exposure regimen, thereby allowing more informative cross-comparisons and meta-analyses to be performed.

One should note that any GCR reference field will cover a broad range of particle types and energies and will likely be represented in the laboratory by a discrete number of (and comparatively few) mono-energetic ion beams. This approximate laboratory representation of a broad, continuous field with discrete beams clearly introduces a modest uncertainty that is difficult to quantify. Variation in the induced tissue field in space associated with shielding configuration and tissue location needs to be viewed within this context (i.e. the variation needs to be larger than the uncertainty associated with discrete beam representation in the laboratory).

Calculations in this paper are performed using the HZETRN transport code [Wilson et al. 1991, Slaba et al. 2010a] including bi-directional neutron transport [Slaba et al. 2010b] along with the π/EM cascade [Norman et al. 2012, 2013; Slaba et al. 2013b]. The GCR spectrum is generated using the 2010 Badhwar-O'Neill GCR model [O'Neill 2010]. June 1976 and 2001 are used as representative dates for solar minimum and maximum conditions, respectively. The Female Adult voxel (FAX) phantom [Kramer et al. 2004] is used to represent human tissue and self-shielding; implementation of the human phantom into HZETRN has been discussed elsewhere [Slaba et al. 2010c]. For dose equivalent and effective dose calculations, the NASA recommended quality factors and tissue weighting factors are used [Cucinotta et al. 2013]. Verification and validation comparisons for the Badhwar-O'Neill GCR model and HZETRN code have been discussed elsewhere [Slaba et al. 2013b; O'Neill et al. 2015; Wilson et al. 2005, 2014, 2015].

In subsequent figures and discussion, the tissue dose equivalents are presented along with the physical quantity, dose. It is recognized that the quality factor used to compute dose equivalent is applicable for carcinogenesis but not for other biological endpoints, such as CNS or cardiovascular effects, which may be of interest. It should be clear after considering the results and discussion in this section that the final conclusions are not dependent on the implementation of the cancer quality factor and dose equivalent. The dose equivalent results are provided as supplemental information in support of the final conclusions.

In the comparisons below, four realistic geometry models are considered along with simplified spherical aluminum shielding with thicknesses of 5 g/cm^2, 20 g/cm^2, and 40 g/cm^2. The realistic geometries are represented by detailed models of the International Space Station (ISS), the Space Transportation System (STS), an adaptation of the Habitat Demonstration Unit (HDU) for a one year free space mission [Walker et al. 2013b], and a Cislunar vehicle [Simon et al. 2014]. The vehicle location considered in ISS is located in the US Lab near the overhead racks. The vehicle location considered in STS is in the middeck and has been referred to as DLOC2 in past publications [Wilson et al. 2003, 2005]. The vehicle location considered in the HDU is in the center of the loft section, and the location in the Cislunar vehicle is on the treadmill, as shown in Figure 4.

In Table 2, female effective dose values are given for solar minimum conditions in each of the shielding geometries, and Figure 5 shows the individual tissue exposures contributing to effective dose. Note that the NASA quality factor for leukemia applied to Blood Forming Organ (BFO) sites has a smaller peak value as compared to the quality factor used for solid cancers in all other tissues [Cucinotta et al. 2013]. This difference has been offset in the figure to improve clarity by multiplying BFO dose equivalent values by 1.6. The value of 1.6 corresponds to the ratio of the BFO dose equivalent values obtained with the solid cancer and leukemia quality factors.

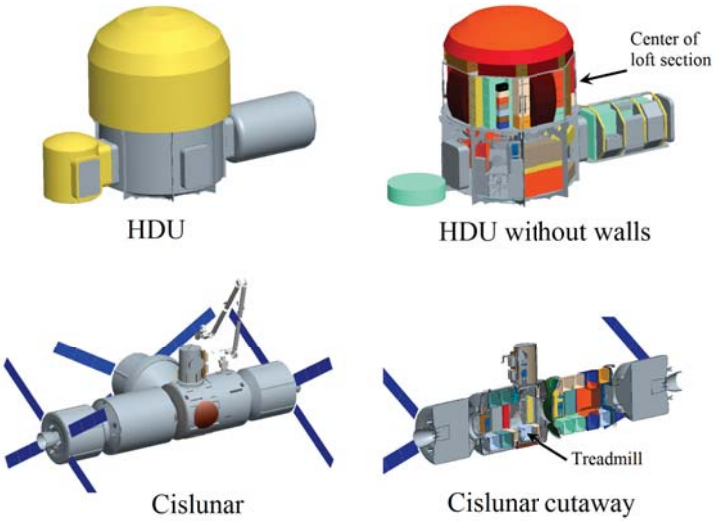

Figure 4. HDU and Cislunar geometries.

Table 2. Female effective dose values (mSv/year) in various shielding geometries during solar minimum.

Shielding	NASA Effective dose
ISS	315.6
STS	368.2
Cislunar	315.2
HDU	327.0
5 g/cm^2 aluminum	397.2
20 g/cm^2 aluminum	335.6
40 g/cm^2 aluminum	320.2

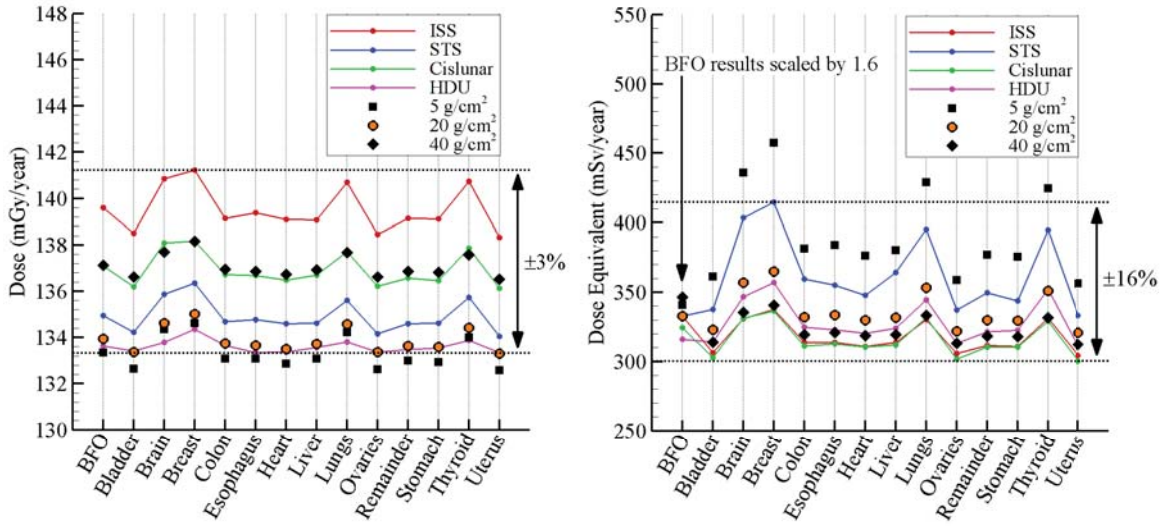

Figure 5. Female tissue dose (left pane) and dose equivalent (right pane) values behind shielding configurations during solar minimum conditions. The BFO dose equivalent values have been scaled 1.6 to offset quality factor differences [Cucinotta et al. 2013] and improve plot clarity.

The variation in total effective dose values in realistic geometries is ±8%. The variation across all tissues and geometries, as shown in Figure 5, is ±3% for dose and ±16% for dose equivalent. Dose equivalent is slightly more sensitive than dose to shielding thickness due to the added emphasis placed on HZE ions by the quality factor. One therefore sees in Figure 5 that greater variation occurs as a function of both shielding geometry and tissue location if dose equivalent is considered. Nonetheless, the variation in exposure quantities caused by shielding geometry and tissue location is small compared to the uncertainties discussed in the beginning of this section. For example, the propagated uncertainty on effective dose associated with modeling just the free space GCR spectrum for a given mission is at least ±20% [Slaba et al. 2014b]. The observed variation is also likely within the uncertainty associated with representing the full reference field by a discrete number of mono-energetic ions beams in the simulator.

It is also worth noticing that as a function of increasing shield thickness, tissue dose values tend to increase while dose equivalent values tend to decrease. The tissue dose is heavily influenced by contributions from hydrogen and helium. The dose versus depth curves from these particles tend to monotonically increase with increasing shield thickness, corresponding to slowing down of the primary beam and added contributions from secondary particles and target fragments with higher LET. The tissue dose equivalent, on the other hand, is more heavily influenced by contributions from HZE particles. The HZE dose equivalent versus depth curves tend to decline noticeably up to moderately thick shielding, corresponding to breakup of the HZE ions into lighter ions and nucleons.

It was found that the bladder and breast results generally bounded all other tissue exposures. The breast has very little self-shielding, resulting in larger exposures, while the bladder is more deeply positioned within the body and well shielded in all directions, resulting in smaller exposures. The BFO results were found to be near the average of all tissue exposures. This can be seen for dose in the left pane of Figure 5. The same conclusion was drawn for dose equivalent if the ICRP 60 [ICRP 1990] quality factor is used in place of the NASA quality factor. The trend for BFO is attributed to the distributed nature of the tissue sites found throughout the body and represented in the computational procedure [Slaba et al. 2010c]. Recognizing that the bladder, BFO, and breast results approximately span the range of exposures found within the body allows subsequent plots and discussion to be simplified and focused. It should also be noted that the results behind simplified spherical shielding approximately cover the range of values set by the complicated shielding geometries.

The results in Table 2 and Figure 5 provide integrated exposure quantities receiving contributions from a range of energies and particles. Figure 6 shows the relative contribution to dose and dose equivalent from charge groups in the bladder, BFO, and breast behind spherical aluminum shielding during solar minimum. Considering the spherical shielding, instead of the complicated geometries, allows the depth-dependence in dose and dose equivalent to be clearly seen. The trends for dose and dose equivalent in Figure 6 are similar, but the presence of the quality factor in dose equivalent again amplifies the relative variation with shielding thickness. In particular, the contribution from $Z > 10$ shows clear depth dependence, corresponding to the breakup of HZE ions as they pass through shielding and tissue. The breast tissue in particular shows this breakup and the compensating buildup in the $Z = 1$ and $Z = 2$ contributions. The results for bladder, BFO, and breast in Figure 6 are qualitatively similar, suggesting that the other tissues will show similar behavior.

It is interesting to note that $Z = 1$ and $Z = 2$ contribute most heavily to both exposure quantities behind moderate shielding. In the BFO behind 20 g/cm^2, the $Z = 1$ and $Z = 2$ particles account for 81% of the dose and 67% of the dose equivalent. Similar results have been shown and discussed elsewhere [Walker et al. 2013a, Norbury and Slaba 2014] and are important to consider when simulator design and beam selection is discussed in more detail later in this paper.

Another quantity of interest is the particle LET spectra [Badavi et al. 2005] occurring in different tissues and shielding configurations, as shown in Figure 7. The numerous peaks appearing in the plot are associated with singularities introduced when transforming flux as a function of kinetic energy into flux as a function of LET. The location of the peaks along the horizontal axis are characteristic of individual ions. For example, the peak occurring near 0.2 keV/μm corresponds to high energy protons (where the proton stopping power versus energy curve has a local minimum). The quantity plotted on the vertical axis, flux, has also been scaled by LET to improve plot clarity. Integrating under the curves shown in Figure 7 yields the total dose (standard constants to convert from MeV/g to Gy would need to be applied).

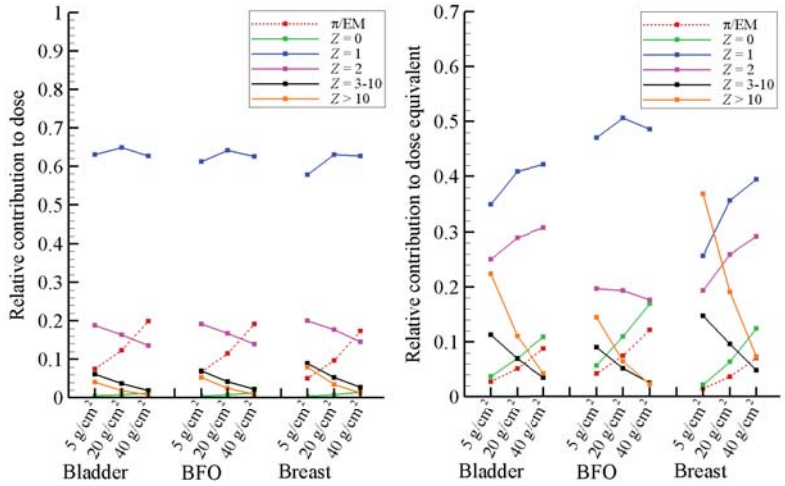

Figure 6. Relative contribution to dose (left pane) and dose equivalent (right pane) from charge groups in the bladder, BFO, and breast behind 5 g/cm^2, 20 g/cm^2, and 40 g/cm^2 spherical aluminum shielding during solar minimum conditions.

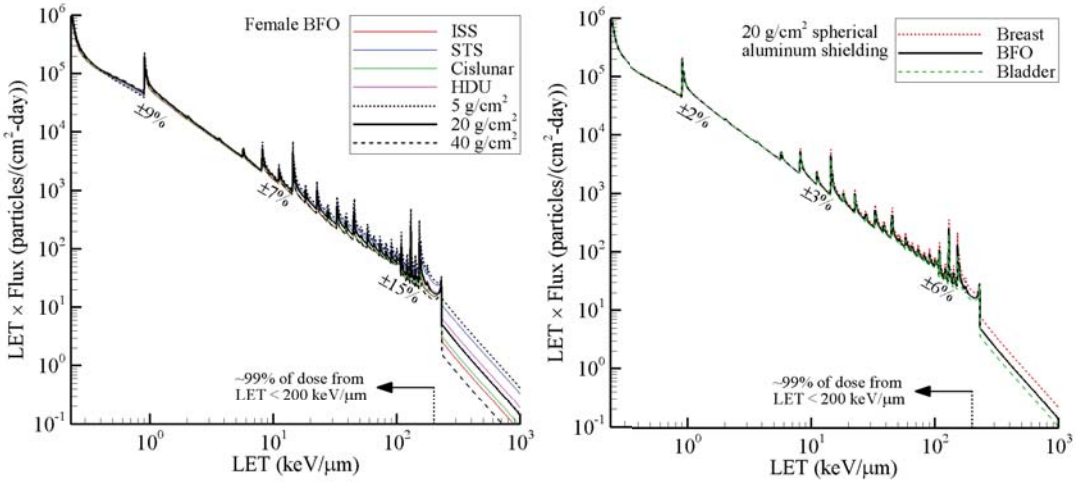

Figure 7. Differential LET spectra in female BFO behind shielding configurations (left pane) and in various tissues behind 20 g/cm^2 aluminum shielding (right pane) during solar minimum conditions. Percent differences indicate the relative variation in spectral results near 1 keV/μm, 10 keV/μm, and 100 keV/μm.

It will be discussed later in the paper that discrete ion and energy beam selection in the GCR simulator can be guided by the tissue LET spectrum behind shielding. The left pane of Figure 7 shows LET spectra in the female BFO behind various shielding configurations, and the right pane shows LET spectra for various tissues behind 20 g/cm^2 of spherical aluminum shielding. The spectra are difficult to discern on the plots, suggesting little variation with shielding configuration or tissue location and consistent with previous results and discussion. Differences can be clearly seen at LET values greater than 200 keV/μm; however, the flux of particles with such high LET is quite small, and therefore, the region does not contribute heavily to dose or dose equivalent. Below 10 keV/μm, a region that contributes heavily to dose and dose equivalent, spectral results are nearly indistinguishable. The variation observed in Figure 7 is within the uncertainty associated with predicting such spectra as derived from comparisons to space measurements [Wilson et al. 2005, Badavi et al. 2009]. The variation is also likely within the ability of the GCR simulator to reproduce such spectra with relatively few discrete mono-energetic beams.

Variation in the induced tissue field: Shielding material

Another factor that may introduce modest variation in exposure estimates is shielding material. Current technologies would indicate that a deep space shielding concept will be comprised heavily of aluminum (or materials with similar shielding properties) with some parasitic shielding used either to augment the existing mass or as a storm shelter [Wilson et al. 1997, Simon et al. 2014]. The parasitic shielding is commonly represented as polyethylene due to the hydrogen content and improved shielding characteristics compared to aluminum, especially for neutrons. In this section, tissue exposure estimates obtained behind aluminum and polyethylene spherical shielding are compared. It is recognized that a deep space shielding concept will not be comprised entirely of polyethylene; the current analysis is meant to provide an approximate bound on the impact of material selection in the shielding configuration. Similar studies have been performed previously, and the variation was found to be small compared to other uncertainties for GCR conditions [Walker et al. 2011].

Results are given in Figure 8 for 20 g/cm^2 of either aluminum or polyethylene spherical shielding. As was the case in Figure 5, when several shielding configurations were considered, there is little variation caused here by different shielding materials. It should be noted that heavier metals like copper, steel, or tungsten would cause increased exposure estimates as compared to aluminum [Walker et al. 2011]; however, it is not likely that a deep space shielding configuration would be heavily composed of such materials.

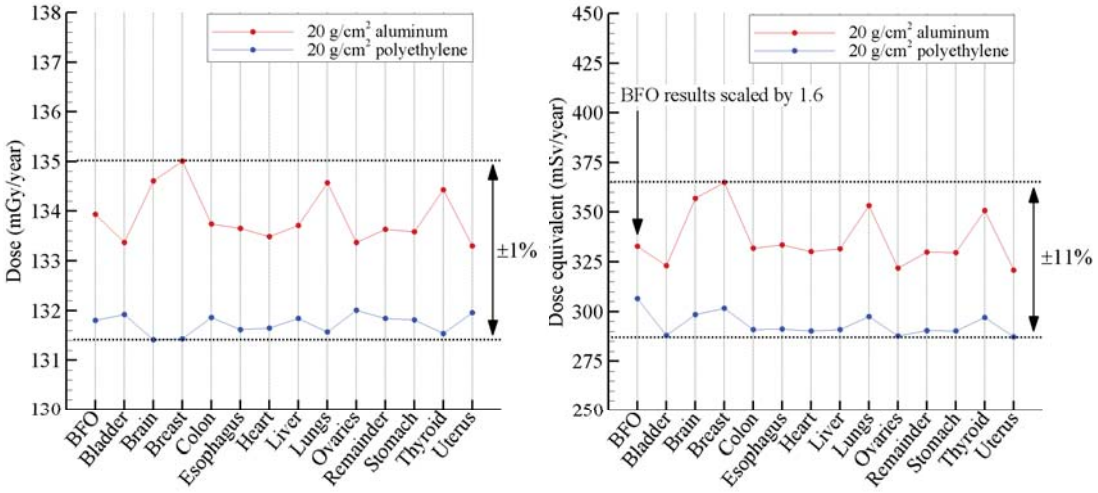

Figure 8. Same as Figure 5 except that results are only shown for 20 g/cm^2 of aluminum and polyethylene spherical shielding.

Variation in the induced tissue field: Solar activity

The last factor contributing to variation in the local tissue field, considered herein, is solar activity. The external GCR field is inversely correlated with the strength of the solar magnetic field and is modulated on an approximate 11 year cycle. The analysis presented thus far has been for solar minimum conditions when the GCR environment is most intense. During solar maximum, the solar magnetic field is at its strongest, resulting in attenuation of the GCR spectrum below several GeV/n. This attenuation suppresses exposure estimates behind shielding by approximately a factor of two, depending on shielding configuration. The variation observed between solar minimum and solar maximum in the local radiation field within tissue and behind shielding will consequently be much larger than what has already been shown and discussed here.

Despite this increased variation, the differences between solar minimum and solar maximum still may not require multiple reference fields. In Figure 9, the LET spectrum in the female BFO behind aluminum shielding during solar minimum and solar maximum conditions is shown. The solar maximum results have been scaled by 1.85. This value was found to minimize the difference between the tissue dose equivalent values behind 20 g/cm^2 of shielding during solar minimum and solar maximum conditions.

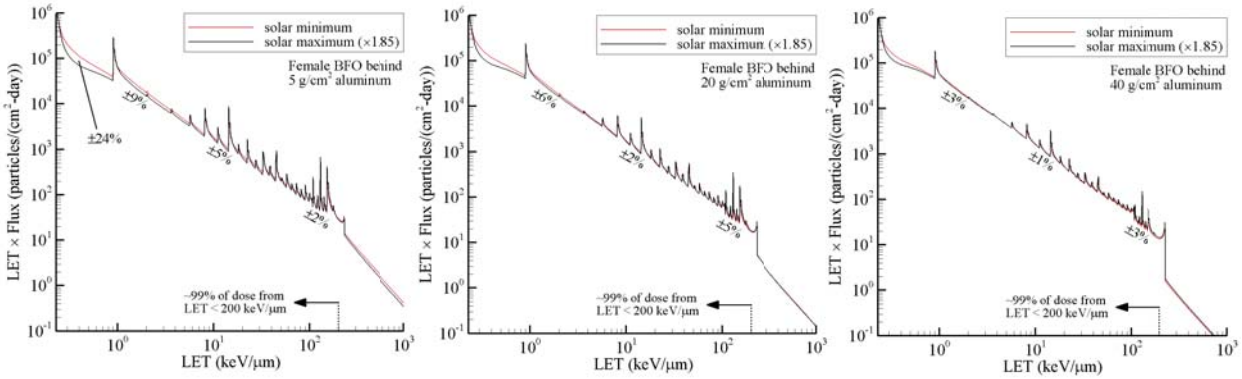

Figure 9. Differential LET spectra in female BFO behind 5 g/cm^2 (left pane), 20 g/cm^2 (middle pane), and 40 g/cm^2 (right pane) of aluminum during solar minimum and solar maximum conditions. The solar maximum results have been scaled by 1.85. Percent differences indicate the relative variation in spectral results near 1 keV/μm, 10 keV/μm, and 100 keV/μm.

Results in Figure 9 suggest that a single scale factor nearly corrects the differences associated with solar activity across the entire LET spectrum and for a range of shielding thicknesses. The largest remaining discrepancies were found below 1 keV/μm, a region which contributes significantly to dose (~50%) and only modestly to dose equivalent (~15%). Though not shown here, it was also found that the single scale factor corrected the differences associated with solar activity to within $\pm$7% for individual tissue dose equivalent values.

Based on these results, it can be concluded that the qualitative differences (i.e. spectral shape and characteristics) induced by solar activity in the local tissue field are minimal, except for the overall magnitude or exposure rate. This implies that a single reference field may still be used to represent both solar extremes, and only the exposure rate needs to be considered as significantly different. The factor of 1.85 could be used in the experimental design to switch between representative exposure rates for solar minimum and solar maximum.

Variation in the induced tissue field: Summary and reference field specification

The analysis and discussion in this section first examined whether simulation of the external, free space environment or the induced tissue field behind shielding is more appropriate given accelerator facility constraints. It was found that simulation of the induced tissue field behind shielding is a more feasible approach at this time. The main drawback of this approach is that the neutron and π/EM components cannot be directly provided within the NSRL beam line. The impact of neglecting these particles in the simulator design (~15% of the exposure) is less severe than the impact of energy constraints associated with simulating the external, free space GCR field directly (~46%-65% of the exposure). More will be said about the neutron and π/EM components later in this paper.

Variation in the induced tissue field behind shielding caused by tissue location and shielding configuration was examined, and it is likely within the uncertainties associated with predicting such quantities. More importantly, the observed variation is also likely within the uncertainty associated with representing any GCR reference field with a discrete number of mono-energetic ions beams. The impact of solar activity was also studied, and as expected, the magnitude of the tissue exposures was found to change substantially between solar minimum and solar maximum. However, it was shown that this variation can be approximately represented by a single scale factor of 1.85, which corrected differences in tissue exposures associated with solar activity to within $\pm$7% over a range of shielding configurations. Differential LET spectra in tissue behind shielding for solar minimum and solar maximum were also shown to be very similar across the entire LET spectrum using the single scale factor. This indicates that the differences associated with solar activity do not impose significant qualitative changes in the induced tissue field to require multiple reference fields to be defined, and thus, a single reference field may be considered.

The radiation field found within the female BFO behind 20 g/cm^2 of aluminum during solar minimum conditions is therefore identified as the reference field for the GCR simulator. Table 2 and Figures 5-9 have shown that this field lies well within the bounds set by other tissues and shielding configurations considered in this analysis and is therefore a representative choice.

The neutron, hydrogen, and helium energy spectra from the reference field are shown in the left pane of Figure 10. The hydrogen spectrum includes protons (^{1}H), deuterons (^{2}H), and tritons, (^{3}H), and the helium spectrum

includes helions (^{3}He) and alphas (^{4}He). The right pane shows the total differential LET spectrum of the reference field and the differential LET spectrum without the hydrogen and helium contributions. The average hits per cell nucleus, dose, and dose equivalent rates are given in Table 3 for various components of the field. Average hits per cell nucleus were computed by assuming a cell nucleus cross sectional area of 100 μm^2 [Curtis and Letaw 1989]. The neutron dose is defined as the energy deposited by heavy ion ($Z > 2$) nuclear target fragments and recoils induced by neutron-nucleus collisions. Neutron dose equivalent is similarly defined, and has an average quality factor of ~20. The neutron-induced light target fragments ($Z \leq 2$) are explicitly transported in computational procedures and recorded separately from the neutron component.

As already noted, dose equivalent is being considered in this work as supplementary information, providing an additional quantity that can be used to characterize features of the reference field. It will be seen in the next section that the beam selection strategy is guided directly by the physical spectra shown in Figure 10, and dose equivalent is used simply as a verification quantity.

The NASA recommended quality factor for computing dose equivalent distinguishes between solid cancers and leukemia by suppressing the peak quality factor value [Cucinotta et al. 2013]. The reference field has been specified for the female BFO behind shielding, for which the leukemia quality factor is applied in risk estimation and in general practice. However, the intent of the reference field is to provide guidance for experimental design of the GCR simulator and should therefore be viewed more broadly as a representative tissue field. The leukemia quality factor is, in general, bounded above by the solid cancer quality factor and bounded below by a quality factor of one (corresponding to dose). Therefore, subsequent dose equivalent calculations will utilize the solid cancer quality factor. Greater emphasis is also placed on the solid cancer results since they account for 80%-90% of the astronaut carcinogenesis risk [Cucinotta et al. 2013].

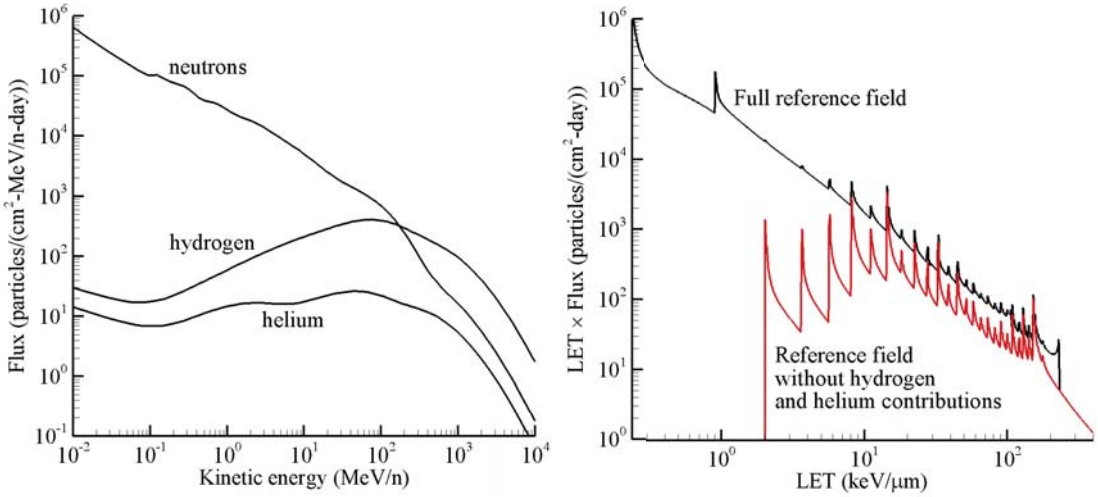

Figure 10. Neutron, hydrogen, and helium energy spectra in the female BFO behind 20 g/cm^2 of aluminum shielding during solar minimum conditions (left pane). The right pane shows the corresponding differential LET spectra with and without contributions from hydrogen and helium.

Table 3. Average hits per cell nucleus per year, dose, D (mGy/year) and dose equivalent, H_{solid} (mSv/year) rates for reference environment during solar minimum along with average quality factors.

	Avg. hits per cell	D	H_{solid}	$\langle Q_{solid} \rangle$
π/EM	0.1	15.5	15.5	1.0
neutron	N/A	1.1	22.9	20.8
hydrogen	126	86.0	131.1	1.5
helium	7	22.5	93.8	4.2
HZE	0.5	8.9	73.3	8.2
Total	134	133.9	336.6	2.5

Sensitivity Analyses

Before implementing procedures to simulate the designated reference field, it is helpful to look more carefully at the particles and energies contributing significantly to the local exposure. This information will aid discrete beam selection in the experimental design. Preliminary results have already been provided in the right pane of Figure 3, where it was shown that energies below 1.5 GeV/n account for ~85% of the effective dose behind shielding. Table 3 provides some additional insight where it is seen that hydrogen and helium dominate the dose (81%) and dose equivalent (67%) of the reference environment. In this section, more detailed analysis is provided regarding the particles and energies in the reference field contributing most significantly to the exposure. This information is then compared against upper energy limitations at NSRL and potential lower energy limitations associated with animal model exposures. Where applicable, quality factor uncertainties have been accounted for using Monte Carlo analysis and parameter uncertainty distributions described by Cucinotta et al. [2013].

Figure 11 shows the relative contribution to dose (left pane) and dose equivalent (right pane) from various particles in the reference field. Note again that values for a specific Z value include contributions from several isotopes. Values for $Z = 1$ include protons, deuterons, and tritons, while values for $Z = 2$ include helions and alphas. It is seen that $Z = 1$ and $Z = 2$ contribute 81% of the total dose and 67% of the total dose equivalent. The HZE contributions are more clearly seen in the inset plots; individual ion contributions are all less than 1% for dose and 6% for dose equivalent. However, the sum of all HZE contributions is more substantial – 7% for dose and 21% for dose equivalent. The small contribution from HZE particles as compared to light ions is a result of nuclear fragmentation events occurring in the shield and tissue. As the overall intensity of the HZE field is attenuated due to breakup of the primary ions, the intensity of the nucleon field builds-up, especially at lower energies.

Despite the reduced contribution of HZE particles behind moderate shielding and tissue, they still need to be represented in the simulated reference field. Figure 11 suggests that of the HZE particles, the contributions from Z = 6, 7, 8, 10, 12, 14, 20, and 26 are amplified compared to other heavy ions. In fact, these ions make up 69% of the HZE dose and 64% of the HZE dose equivalent. Another important aspect of Figure 11 is the contributions from neutrons and the π/EM cascade. The neutrons contribute approximately 1% to dose and 7% to dose equivalent, while the π/EM cascade contributes 11% to dose and only 5% to dose equivalent. These particles cannot be directly simulated in the NSRL beam line.

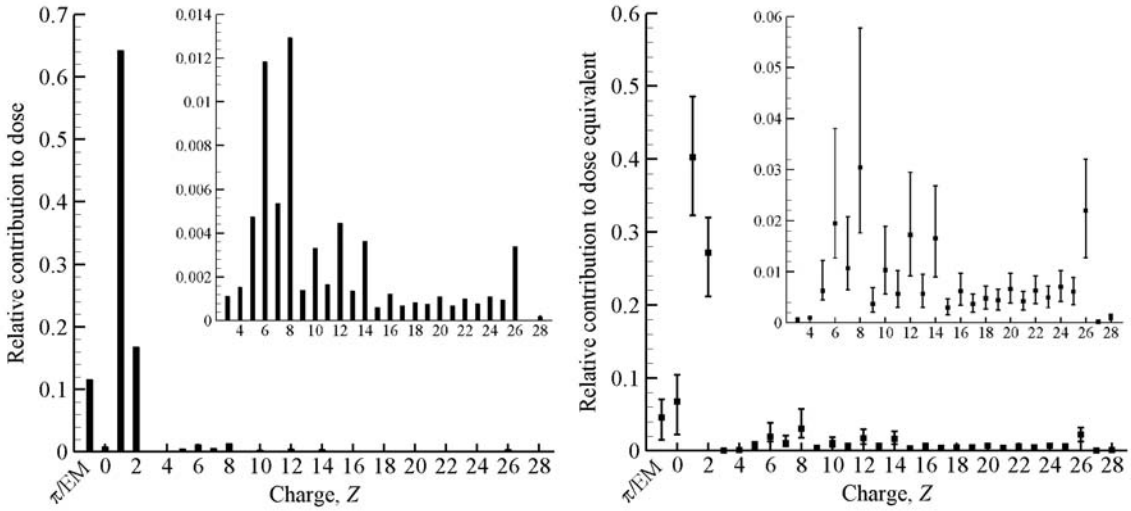

Figure 11. Relative contribution to dose (left pane) and dose equivalent (right pane) from particles in reference field. Inset plots have the vertical axis zoomed-in to improve clarity for HZE contributions. Symbols and error bars in dose equivalent plot correspond to median and 95% confidence level values, respectively.

Table 4 gives the dose and dose equivalent from selected Z values in the reference field. The contributions from energies within current NSRL constraints, which allow protons up to 2.5 GeV and alphas up to 1 GeV/n, are explicitly separated. The data in Table 4 are consistent with results shown previously in the right pane of Figure 3 for a related exposure quantity (effective dose). In general, the current energy constraints provide a reasonably

complete representation of the local tissue field. It is interesting to note however that the energy constraints for Z > 2 impose some modest limitations on representing the local tissue field. Approximately 41% of the HZE dose is delivered by energies greater than 1 GeV/n. However, the total contribution from HZE particles to dose is only 7%, as shown in Table 3, and the high energy heavy ions contribute a smaller amount (~27%) to the HZE dose equivalent.

Table 4. Dose (mGy/year) and dose equivalent (mSv/year) for selected ions in the reference field. E_{lim} is the current upper energy limit at NSRL. E_{lim} = 2.5 GeV for Z = 1, and E_{lim} = 1.0 GeV/n for all Z > 1.

Z	Dose			Dose Equivalent		
	Total	$E < E_{lim}$	Fraction	Total	$E < E_{lim}$	Fraction
1	86.0	77.3	0.90	131.1	120.0	0.92
2	22.5	19.1	0.85	93.8	90.0	0.96
6	1.58	1.00	0.63	6.19	5.43	0.88
7	0.72	0.45	0.63	3.42	3.01	0.88
8	1.73	1.06	0.61	9.83	8.57	0.87
10	0.44	0.26	0.59	3.41	2.88	0.85
12	0.59	0.34	0.57	5.85	4.74	0.81
14	0.49	0.27	0.55	5.80	4.40	0.76
20	0.14	0.08	0.53	2.53	1.60	0.63
26	0.45	0.22	0.50	8.82	4.52	0.51
All Z > 2	8.9	5.3	0.59	73.3	53.7	0.73

Another point to consider before developing beam selection strategies is the impact of any shielding provided by the biological target. For mouse models, the self-shielding of the animal may significantly slow or stop the primary beam ions. It could be argued that primary ion stoppage, or so-called Bragg peaks, should be avoided in the simulator to prevent highly localized tissue response and rapid exposure gradients from occurring within the animal. These localized responses would be difficult to reproduce in subsequent experiments if animals are allowed to move within the confinement units. On the other hand, lower energy, high LET, particles that stop within tissue contribute significantly to the overall exposure and should be considered.

It is therefore instructive to get some estimates on the beam energies needed to pass through the animal without stopping and the possible impact of neglecting the lower energy particles in beam selection. For this, and subsequent analysis in this paper, it is assumed that the mouse is represented by an ellipsoidal phantom with axial length of 7 cm and a minor diameter (along the y and z-axes) of 3 cm (see Figure 12). These dimensions produce a phantom mass of 33 grams, assuming a water phantom with a density of 1 g/cm^3.

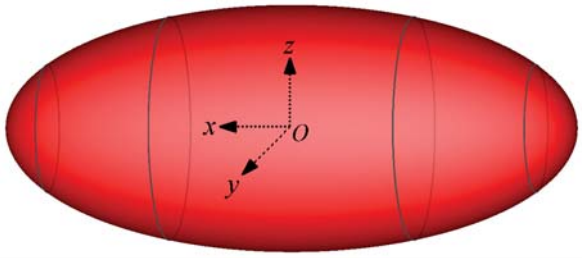

Figure 12. Ellipsoidal mouse phantom. The length along the x-axis is 7 cm, and the minor axis lengths (measured along the y and z-axes at x = 0) are 3 cm.

Table 5 gives the energies needed by selected ions to reach 9 cm, 25 cm, and 80 cm. The distance of 9 cm (instead of the phantom distance of 7 cm) is used to cover most nose-to-base of tail dimensions for mice, with extra margin included to account for physical phenomena that may alter the projected range of ions such as multiple scattering, range straggling, elastic collisions, and bone/tissue density modifications. The distances of 25 cm and 80 cm are related to approximate dimensions of larger animals such as rats and minipigs, respectively.

The energies needed to reach 9 cm (most mice) are met within current facility constraints, thereby allowing primary ion Bragg peaks to be avoided in the animals, if desired. The energies needed to reach 25 cm (rat proxy) are also met within current facility constraints, but for the heaviest ions, substantial energies are needed to avoid internal Bragg peaks. Finally, the energies needed to reach 80 cm (minipig proxy) are beyond current NSRL capabilities, limiting the applicability of larger animals in the proposed simulator design. It should also be noted that, in the absence of a nuclear collision, an ^{56}Fe ion with kinetic energy of 475 MeV/n will pass through most mice without stopping but will be slowed significantly, leaving an inhomogeneous energy deposition profile along its path. In the following section, the exposure profile within the ellipsoidal phantom is examined to address this concern.

Table 5. Beam energy (MeV/n) needed to reach 9 cm, 25 cm, and 80 cm.

	Energy (MeV/n) need to reach distance		
	9 cm	25 cm	80 cm
^{1}H	109	195	393
^{4}He	109	195	393
^{12}C	204	377	806
^{14}N	224	415	898
^{16}O	242	452	987
^{20}Ne	277	521	1166
^{24}Mg	308	587	1336
^{28}Si	339	650	1499
^{56}Fe	475	946	2334

Beam Specification

In this section, an approach for selecting discrete beams (ions, energies, and intensities) to approximately represent the reference environment, as given in Table 3 and Figure 10, is described. The information gathered in the previous sections regarding importance of specific ions and energy constraints is taken into account where possible.

A summary of the overall approach follows. The hydrogen and helium energy spectra are represented by mono-energetic proton and alpha beams, respectively. Lower energy particles that will stop within the mouse phantom are included in this part of the problem by utilizing the NSRL polyethylene beam degrader system [NSRL 2015]. Sensitivity studies are provided to show that the NSRL polyethylene beam degrader system allows such an approach to be implemented without inducing rapid internal exposure gradients. It is recognized that the reference field hydrogen spectrum contains contributions from ^{2}H and ^{3}H, which may produce distinct biological responses compared to just protons. A similar statement can also be made for the ^{3}He component of the helium spectrum. However, protons account for 97% of the hydrogen reference field flux, and alphas account for 88% of the helium reference field flux. The approximate representation of the reference field hydrogen and helium spectra with protons and alphas, respectively, is therefore reasonable.

The HZE ions are collectively represented by considering the associated LET spectrum (see red curve in the right pane of Figure 10). In this part of the problem, the lower energy limitations given in Table 5 for a distance of 9 cm are also incorporated so that localized tissue responses and rapid exposure gradients within mouse models are avoided. The larger distance of 9 cm, instead of the phantom distance of 7 cm, is being used so that the beam specification strategy is more broadly applicable to mice commonly used in radiobiology studies.

The first sub-section gives a general description of the beam selection strategy, with specific choices made to provide some clarity. The second sub-section examines the number of low-energy bins needed for hydrogen and helium to provide reasonably smooth exposure gradients within a mouse phantom. The final sub-section evaluates various exposure quantities induced by the discrete beam selection and compares these results to the corresponding reference field quantities as a verification of the proposed strategy.

General beam selection strategy

Figure 13 depicts the general strategy for selecting discrete mono-energetic ion beams to represent the reference field. As has already been shown and discussed, hydrogen and helium account for a large fraction of the total exposure in the reference field. The energy spectra of these two ions are therefore explicitly considered in this strategy, as shown in the left pane of Figure 13. Note that even the lower energy portions of the hydrogen and helium spectra are being considered (i.e. the energies that will likely stop in a mouse). It will be shown later that the

NSRL polyethylene beam degrader system allows for an efficient energy switching capability with enough resolution to ensure reasonably smooth exposure profiles within the animal target. The HZE ions are collectively represented within the LET spectrum of the reference field (without hydrogen and helium contributions), as shown in the right pane of Figure 13. For these particles, lower energy constraints associated with animal phantom are applied (i.e. energies selected to ensure ion reaches at least 9 cm).

Alternatively, one could explicitly represent the energy spectrum of specific HZE ions, such as C, O, or Fe, using the methods outlined here for hydrogen and helium. The flux of particles directly represented in the energy domain would then need to be subtracted from the remaining LET spectrum to avoid double counting. However, it should be noted that full energy spectral resolution for additional ions (beyond hydrogen and helium) greatly increases the number of mono-energetic beams needed directly from the accelerator facility. Such decisions would need to be weighed against facility limitations for rapid ion and energy switching. The current choice of considering hydrogen and helium seems justified from the analysis provided thus far and is within current NSRL switching capabilities.

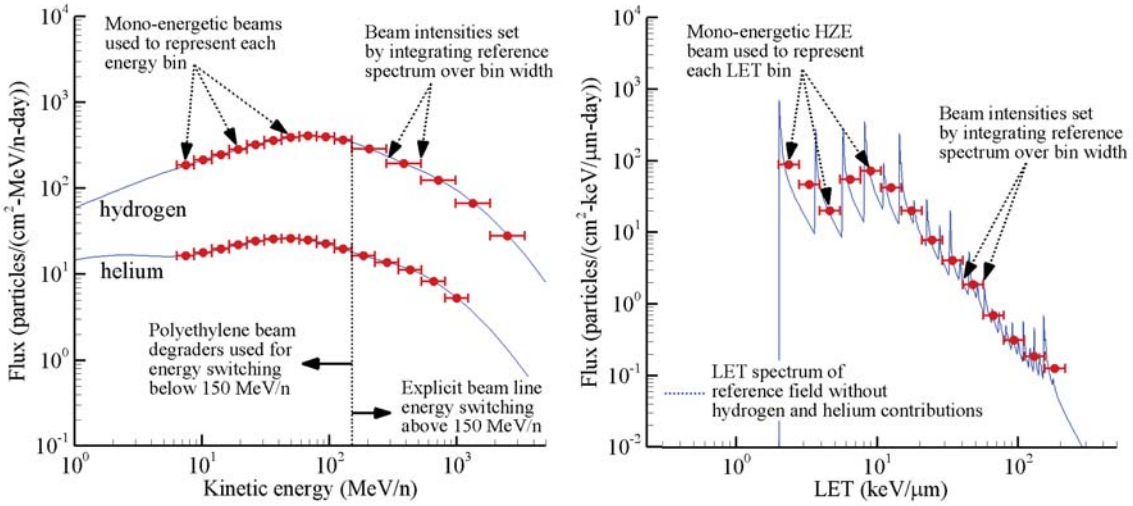

Figure 13. General strategy for representing the reference field with discrete mono-energetic beams. The hydrogen and helium energy spectra are considered directly (left pane), while HZE ions are represented within the LET spectrum (right pane). Solid blue lines are the reference spectra from Figure 10.

For hydrogen and helium, the energy domain has been separated into discrete log-spaced bins above and below 150 MeV/n. Each energy bin will be represented by a mono-energetic beam. Below 150 MeV/n, discrete proton and alpha beam energies are achieved by using the polyethylene degrader system (presumably using a 150 MeV/n beam as a starting point) [NSRL 2015]. Above 150 MeV/n, proton and alpha beams are delivered directly by the accelerator at the indicated energies (bin mid-point identified with circular symbols). The highest energy bin has been centered at 2.5 GeV for protons and 1.0 GeV/n for alphas, consistent with current NSRL energy limitations. Each beam intensity is determined by integrating the reference field over the indicated energy bin, yielding bin-integral flux in units of particles/(cm^2-day). Since proton and alpha energies below 109 MeV/n might stop in a mouse phantom (see Table 5), convergence testing must be performed to see how many low-energy bins are required to achieve reasonably smooth exposure profiles within the phantom. This will be examined in the following sub-section.

For the HZE ions, the LET domain has been separated into 14 discrete, log-spaced bins. Each LET bin shown in the right pane of Figure 13 will be represented by a mono-energetic HZE ion beam, with the corresponding intensity determined by integrating the reference field over the indicated LET bin, again yielding bin-integral flux in units of particles/(cm^2-day). The ion species and energy specified for a given LET bin is determined by first considering the geometric midpoint of each bin as a representative LET value. In general, there are multiple ions and energies that may produce a given LET value, but imposing the upper and lower energy limits discussed in the previous section greatly reduces the number of overlapping possibilities. For example, consider the bin centered at ~9 keV/μm. As shown in Table 6, only ^{11}B and ^{12}C have energies that fall within NSRL constraints and will not stop within the animal phantom. Due to the increased importance of ^{12}C compared to ^{11}B, as shown in the previous

section, the LET bin centered at ~9 keV/μm will be represented by ^{12}C at 886.8 MeV/n in this example. A similar analysis was performed for the other bins.

Table 6. Ions and energies with an LET of ~9 keV/μm.

Particle	Energy (MeV/n)
^{1}H	4.8
^{4}He	27.1
^{7}Li	74.9
^{9}Be	164.6
^{11}B	343.9
^{12}C	886.8
^{12}C	21552.2

It can be seen in the left pane of Figure 13 that some regions of the energy domain are not covered by the designated binning structure. The lowest hydrogen and helium energies, below ~10 MeV/n, cannot be resolved within the current fidelity (0.025 cm) of the polyethylene degrader system at NSRL. The highest hydrogen and helium energies, above 2.5 GeV and 1.0 GeV/n, respectively, are above current NSRL energy limitations. Offsetting this problem is the fact that the missing regions do not represent major contributions to the overall exposure. The lowest energy hydrogen and helium ions will barely penetrate the skin of an animal model (or plastic cell culture dish) and therefore contribute negligibly to the exposure at internal tissue sites of interest. The highest energy hydrogen and helium ions have already been shown in the right pane of Figure 3 and in Table 1 to account for less than 10% of the local exposure.

Beam selection information corresponding to Figure 13 is given in Appendix A. The general process for selecting discrete beams to represent the hydrogen and helium energy spectra and remaining HZE ion LET spectrum has now been described. This process results in a very precise particle, energy, and beam intensity specification that is directly related to the reference field flux. It should be clear that this methodology allows for systematic improvements by simply increasing the number of energy or LET bins. The next sub-section examines how many low-energy bins are needed for hydrogen and helium to ensure that reasonably smooth exposure gradients are induced within the animal phantom.

Low energy convergence testing

In the general beam selection strategy outlined in the previous sub-section, the hydrogen and helium energy spectra below 150 MeV/n were represented by discrete energy beams achieved by using polyethylene degraders. Many of the slowed-down beams emerging from the degrader system are likely to stop in a mouse phantom, leaving a series of rapidly changing internal exposure profiles. This effect can be mitigated by increasing the number of low energy bins used to represent the reference field – essentially creating a spread out Bragg peak. In this section, convergence testing is performed to provide some general guidance on how many low energy bins are needed to achieve smooth internal exposure profiles.

To examine this problem, the mouse phantom discussed previously (tissue ellipsoid with axial length 7 cm and a 3 cm primary diameter) is exposed isotropically to mono-energetic proton beams. The beam energies and intensities are specified using the binning procedure outlined in the previous section. Figure 14 shows the resulting internal exposure profiles as the number of energy bins is increased from 3 to 25. As the number of bins is increased, it is clear the internal variation is reduced, and no significant internal gradients, or hot-spots, are observed if at least 10 energy bins are used (as in the left pane of Figure 13). It was found that increasing the number of bins beyond 25 had little impact on further reducing the internal variation. Additionally, if more than 25 bins are considered, extra analysis is required to ensure all of the lowest energy bins can be generated within the fidelity of the polyethylene degrader system at NSRL (0.025 cm). A similar analysis was performed for alpha beams to represent the low energy portion of the reference helium spectrum with qualitatively similar results. In the next section, various exposure quantities induced by the discrete beam selection are compared to reference field quantities to provide general verification of the proposed strategy.

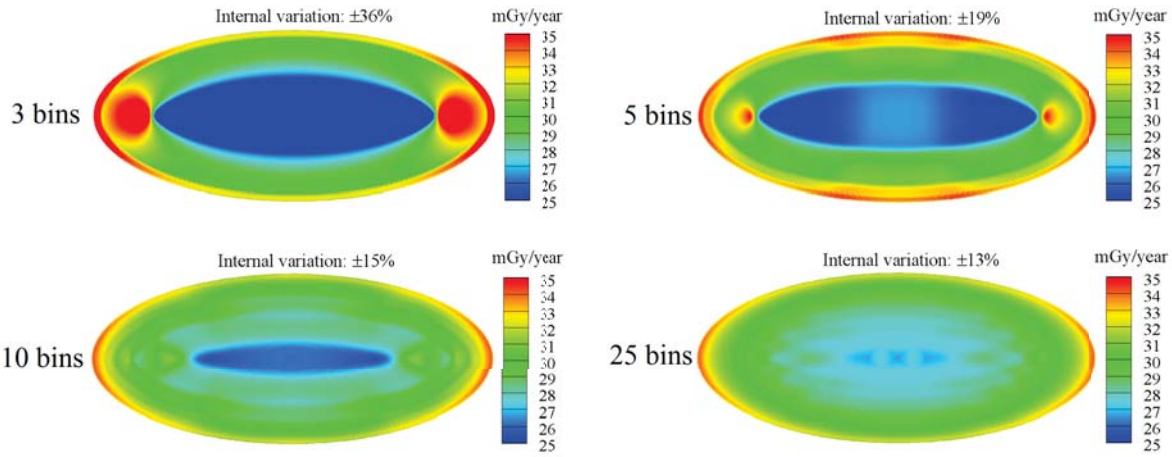

Figure 14. Internal exposure profiles in ellipsoidal mouse phantom exposed to isotropic radiation boundary condition. The boundary condition is represented as a series of mono-energetic proton beams with energies and intensities set by binning the reference field hydrogen energy spectrum with the indicated number of bins.

Verification of Reference Quantities with Discrete Beams

In this section, the beams identified in Appendix A and shown in Figure 13 are used to evaluate various exposure quantities. These values are then compared to corresponding reference field quantities to provide verification of the proposed beam selection strategy. Spectral quantities computed at the center of the ellipsoidal phantom exposed isotropically to the discrete beams are shown in Figure 15 and compared to the reference field quantities. The LET spectra from the reference field and the beams is shown in the left pane; overall good qualitative agreement is found.

The right pane of Figure 15 provides a similar comparison but for the track structure parameter spectrum [Cucinotta et al. 2013]. The track structure parameter, $X_{tr} = (Z^*/\beta)^2$, has been presented as an improved descriptor of track structure effects, compared to LET alone, and is the basis for revised NASA quality factors and risk assessment models [Cucinotta et al. 2013]. Comparing a different spectral quantity, such as $F(X_{tr})$, provides a somewhat independent assessment on how well the proposed strategy represents quantities of interest to space radiation applications and risk assessment [Cucinotta et al. 2013]. The beams were also not chosen to specifically reproduce $F(X_{tr})$. Good qualitative agreement is found between the reference field spectrum and induced beam spectrum.

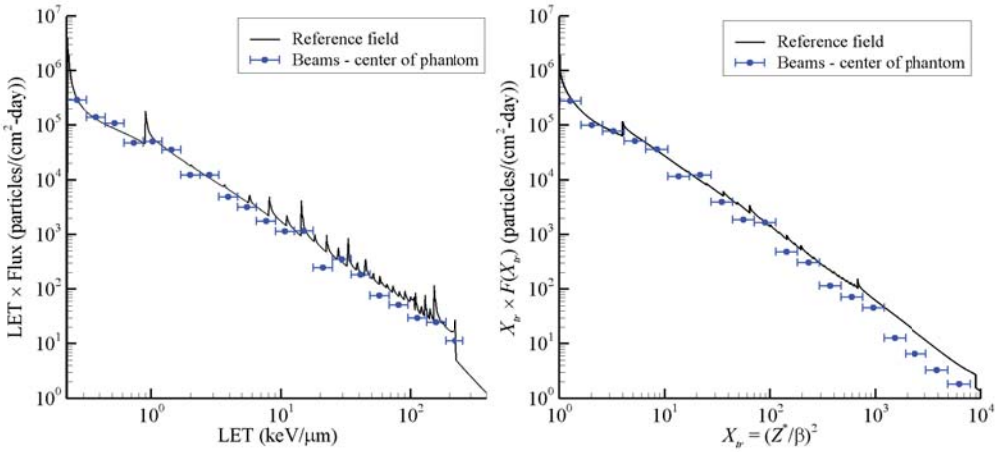

Figure 15. LET spectrum (left pane) and the track structure parameter ($X_{tr} = (Z^*/\beta)^2$) spectrum (right pane) of the reference field compared to the spectrum induced by discrete beams at the center of the phantom.

Figure 16 shows the exposure profiles in a cross sectional plane at $z = 0$ (i.e. *xy* plane) in the ellipsoidal phantom exposed isotropically to the discrete beam selection. Internal variation of dose and dose equivalent values is less than $\pm$10%, showing that discrete beam selection has not led to substantial hot-spots within the phantom. The slight exception to this occurs near the front and back of the phantom, where localized areas of amplified exposures are observed (seen as red-spots on the left and right of each ellipse in Figure 13). It is important to note that this localized behavior is actually quite small (<10% relative variation) and is highly dependent on the geometry and irradiation conditions considered herein. Actual internal profiles will vary based on the size and orientation of the mouse model with respect to the beam.

Table 7 gives various exposure values computed from the beam exposures at the center of the phantom. Reference field values from Table 3 are also given for comparison. All of the beam-induced quantities are reasonably close to the reference field quantities. Clearly, the proposed beam specification strategy provides a reasonably accurate representation of the ion components of the reference field, even with relatively few beams.

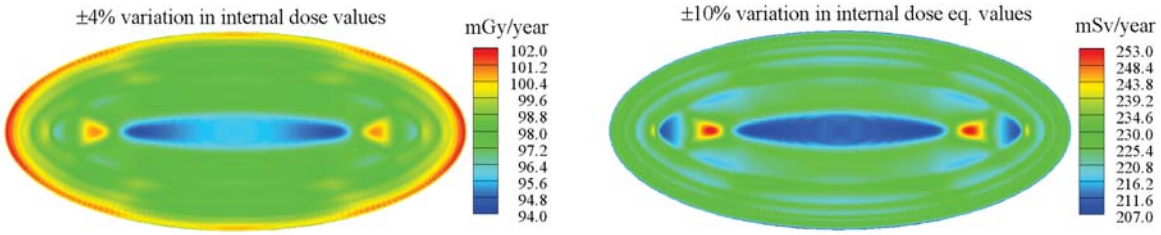

Figure 16. Dose (left pane) and dose equivalent (right pane) contours in animal phantom exposed to discrete beams (isotropic irradiation).

Table 7. Average hits per cell nucleus per year, dose, D (mGy/year), dose equivalent, H_{solid} (mSv/year), and average quality factor, $<Q_{solid}>$ from beam exposures at center of the phantom (isotropic irradiation). Reference field values from Table 3 are also given for comparisons.

		Avg. hits per cell	D	H_{solid}	$<Q_{solid}>$
hydrogen	Ref. field	126	86.0	131.1	1.5
	Phantom center	105	71.6	96.2	1.3
helium	Ref. field	7	22.5	93.8	4.2
	Phantom center	5	16.4	50.0	3.0
HZE	Ref. field	0.5	8.9	73.3	8.2
	Phantom center	0.3	8.3	65.5	7.9
Total	Ref. field	134	133.9	336.6	2.5
	Phantom center	114	96.4	212.3	2.2

Summary and Conclusions

In this paper, two specific aspects of experimental design for simulating the GCR environment in a laboratory setting were examined: reference field specification and preliminary beam selection strategy. First, comparisons were made between two basic experimental setups. In the external field approach, beams are selected to represent the free-space, external GCR field, and the biological target is placed behind a shielding material in the beam line. The shielding material is intended to modify the primary beams in a manner similar to vehicle or habitat shielding for a deep space mission. In the local tissue field approach, models are used to predict the spectrum of particles and energies occurring in a representative tissue behind shielding on a deep space mission. This modified spectrum is then represented in the accelerator with discrete mono-energetic beams and fired directly onto a biological target, with no intervening shield material. Analysis showed that current (and upgraded) NSRL upper energy constraints limit the feasibility of simulating the external, free space GCR spectrum directly. In particular, it was shown that approximately half of the exposure behind shielding is lost if the energies above ~1.5 GeV/n are not represented in the external field. Conversely, it was also shown that the shielded, local tissue environment can be reasonably well represented within current facility limitations which allow protons up to 2.5 GeV and heavier ions up to 1.0 GeV/n. It was therefore concluded that the local tissue field approach is preferable.

Next, a broad set of shielding configurations, including complex vehicles and habitats and simplified spherical shielding, were considered to quantify variability in the induced tissue field behind shielding. It was determined that the observed variability was likely within the uncertainty associated with representing any broad space environment with relatively few mono-energetic beams in the laboratory. This indicated that a single reference environment could be identified. The reference environment was chosen as the female BFO spectrum behind 20 g/cm^2 of shielding during solar minimum conditions.

Finally, a general beam selection strategy was described. Sensitivity studies have shown that hydrogen and helium account for a larger fraction of the overall fluence, dose, dose equivalent, and cell hits in a shielded tissue environment. Consequently, these particles are given greater emphasis in the beam selection strategy. The hydrogen and helium energy spectra are approximately represented with a discrete set of mono-energetic proton and alpha beams, respectively. Below 150 MeV/n the polyethylene beam degrader system is used to provide rapid energy switching, thereby allowing suitably fine energy resolution to avoid inducing rapid exposure gradients within animal models (~spread out Bragg peak). Above 150 MeV/n, proton and alpha energies are provided directly from the beam line. The remaining HZE ions are collectively represented in the LET domain using a binning scheme. For hydrogen, helium, and HZE ions, the proposed strategy allows for precise beam selection criteria that can be systematically improved by simply increasing the number of energy or LET bins. In particular, the proposed strategy ties each beam intensity directly to the reference field flux. Comparisons were made between various reference field quantities and the same quantities induced by discrete beams at the center of an ellipsoidal phantom. Spectral quantities were in good qualitative agreement, and integrated exposure values were quantitatively similar.

A drawback of the proposed strategy is that the neutron and π/EM components of the reference field are not explicitly accounted for. The discrete beams will induced some secondary neutron production as a result of beam interactions with intervening tissue shielding; however, the resulting neutron spectrum found within a mouse phantom is not expected to be qualitatively or quantitatively similar to the reference field neutron spectrum. The π/EM is even more heavily constrained in that the discrete beams available at NSRL are generally not energetic enough to induce a significant cascade. Nonetheless, the neutron and π/EM components, combined, account for less than 15% of the total exposure (dose or dose equivalent). Further study and development is needed to determine methods for representing these components in the simulator.

The results, discussion, and analysis presented herein is highly focused on two specific aspects of simulator design. A variety of other topics need to be examined, such as timing and ordering of beam exposures before final implementation is achieved. Nonetheless, the present results provide some initial guidance to aid in further simulator design.

Acknowledgements

This work was supported by the Human Research Program under the Human Exploration and Operations Mission Directorate of NASA

Appendix

This section provides details for the specific beams used to represent the reference field quantities, as shown in Figure 13. Table A1 gives the information for the beams used to represent the hydrogen energy spectrum from the reference field. Table A2 gives the information for the beams used to represent the helium energy spectrum from the reference field. Table A3 gives the information for the beams used to represent the HZE LET spectrum from the reference field. It is worth noting that the totals from Tables A1 – A3, agree reasonably well with the components given in Table 3.

Table A1. Particles, energies (MeV/n), LET (keV/μm), X_{tr} values, intensities (particles/(cm^2-year)), doses (mGy/year), and dose equivalents (mSv/year) used to reproduce the hydrogen reference energy spectrum. The symbol * in the energy column denotes those beams utilizing polyethylene degraders.

A	Z	Energy	LET	X_{tr}	Intensity	Dose	Dose Eq.
1	1	7.4*	6.4	63.8	1.59×10^5	1.48	1.87
1	1	10.2*	5.0	46.7	2.54×10^5	1.83	2.08
1	1	14.0*	3.8	34.3	4.01×10^5	2.25	2.40
1	1	19.2*	3.0	25.2	6.31×10^5	2.73	2.83
1	1	26.4*	2.3	18.6	9.84×10^5	3.30	3.36
1	1	36.2*	1.8	13.7	1.51×10^6	3.91	3.95
1	1	49.6*	1.4	10.2	2.24×10^6	4.52	4.54
1	1	68.0*	1.1	7.7	3.20×10^6	5.02	5.03
1	1	93.3*	0.8	5.8	4.31×10^6	5.30	5.31
1	1	128.1*	0.7	4.4	5.44×10^6	5.31	5.31
1	1	205.0	0.5	3.1	1.36×10^7	9.62	9.62
1	1	383.2	0.3	2.0	1.72×10^7	8.53	8.53
1	1	716.0	0.3	1.5	2.07×10^7	7.99	7.99
1	1	1337.9	0.2	1.2	2.08×10^7	7.04	7.04
1	1	2500.0	0.2	1.1	1.63×10^7	5.35	5.35
Totals					1.08×10^8	74.18	75.22

Table A2. Particles, energies (MeV/n), LET (keV/μm), X_{tr} values, intensities (particles/(cm^2-year)), doses (mGy/year), and dose equivalents (mSv/year) used to reproduce the helium reference energy spectrum. The symbol * in the energy column denotes those beams utilizing polyethylene degraders.

A	Z	Energy	LET	X_{tr}	Intensity	Dose	Dose Eq.
1	1	7.4*	25.6	255.2	1.42×10^4	0.53	2.18
1	1	10.2*	19.8	186.9	2.10×10^4	0.61	1.66
1	1	14.0*	15.4	137.0	3.21×10^4	0.72	1.41
1	1	19.2*	11.9	100.7	4.94×10^4	0.86	1.30
1	1	26.4*	9.2	74.2	7.42×10^4	0.99	1.27
1	1	36.2*	7.1	54.9	1.08×10^5	1.12	1.28
1	1	49.6*	5.5	40.9	1.49×10^5	1.20	1.30
1	1	68.0*	4.3	30.6	1.97×10^5	1.23	1.29
1	1	93.3*	3.4	23.2	2.45×10^5	1.21	1.24
1	1	128.1*	2.7	17.7	2.92×10^5	1.14	1.16
1	1	185.2	2.1	13.2	4.72×10^5	1.43	1.44
1	1	282.3	1.6	9.8	6.02×10^5	1.41	1.41
1	1	430.3	1.3	7.5	7.52×10^5	1.41	1.41
1	1	656.0	1.1	6.1	8.39×10^5	1.33	1.33
1	1	1000.0	1.0	5.2	8.16×10^5	1.16	1.16
Totals					4.66×10^6	16.34	20.84

Table A3. Particles, energies (MeV/n), LET (keV/μm), X_{tr} values, intensities (particles/(cm^2-year)), doses (mGy/year), and dose equivalents (mSv/year) used to reproduce the HZE reference LET spectrum.

A	Z	Energy	LET	X_{tr}	Intensity	Dose	Dose Eq.
7	3	736.4	2.4	13.1	2.54×10^4	0.09	0.09
7	3	331.4	3.3	19.8	1.87×10^4	0.09	0.09
7	3	189.2	4.6	29.3	1.13×10^4	0.08	0.08
11	5	788.1	6.4	35.5	4.37×10^4	0.41	0.52
12	6	886.8	9.0	48.9	7.89×10^4	1.03	1.53
12	6	365.0	12.6	74.7	6.44×10^4	1.18	2.52
16	8	644.3	17.5	98.7	4.33×10^4	1.11	3.06
16	8	306.2	24.5	148.3	2.35×10^4	0.84	3.98
23	11	589.9	34.2	194.2	1.70×10^4	0.85	5.38
28	14	988.2	47.8	256.9	1.10×10^4	0.76	6.54
32	16	755.4	66.7	369.4	5.71×10^3	0.55	7.30
39	19	781.4	93.2	514.0	3.57×10^3	0.48	8.53
47	22	682.3	130.1	728.1	2.96×10^3	0.56	12.27
56	26	682.4	181.8	1016.8	2.81×10^3	0.74	17.42
Totals					3.52×10^5	8.77	69.29

References

Badavi, F.F., Wilson, J.W., Hunter, A., Numerical study of the generation of linear energy transfer spectra for space radiation applications. NASA TP 2005-213941, 2005.

Badavi, F.F., Xapsos, M.A., Wilson, J.W., An analytical model for the prediction of a micro-dosimeter response function. *Adv. Space Res.* **44**: 190-201, 2009.

Clowdsley, M.S., Nealy, J.E., Atwell, W., Anderson, B.M., Luetke, N.J., Wilson, J.W., Calculation of radiation protection quantities and analysis of astronaut orientation dependence. AIAA Space 2006 conference, AIAA 2006-7441, 2006.

Cucinotta, F.A., Townsend, L.W., Wilson, J.W., Shinn, J.L., Badhwar, G.D., Dubey, R.R., Light ion components of the galactic cosmic rays: nuclear interactions and transport theory. *Adv. Space Res.* **17**: 277-286, 1996a.

Cucinotta, F.A., Wilson, J.W., Shinn, J.L., Badavi, F.F., Badhwar, G.D., Effects of target fragmentation on evaluation of LET spectra from space radiations: implications for space radiation protection studies. *Radiat. Meas.* **26**: 923-934, 1996b.

Cucinotta, F.A., Kim, M.Y., Chappell, L.J., Space radiation cancer risk projections and uncertainties – 2012. NASA TP 2013-207375, 2013.

Curtis, S.B. and Letaw, J.R., Galactic cosmic rays and cell-hit frequencies outside the magnetosphere. *Adv. Space Res.* **9**: 293-298, 1989.

Durante, M., Kraft, G., O'Neill, P., Reitz, G., Sabatier, L., Schneider, U., Preparatory study of a ground-based space radiobiology program in Europe. *Adv. Space Res.* **39**: 1082-1086, 2007.

ICRP, 1990 Recommendations of the International Commission on Radiological Protection. ICRP Publication 60, 1990.

Kramer, R., Vieira, J.W., Khoury, H.J., Lima, F.R.A., Loureiro, E.C.M., Lima, V.J.M., Hoff, G., All about FAX: A female adult voxel phantom for Monte Carlo calculations in radiation protection dosimetry. *Phys. Med. Biol.* **49**: 5203-5216, 2004.

NCRP, Information needed to make radiation protection recommendations for space missions beyond low-earth orbit. NCRP Report 153, 2006.

NCRP, Uncertainties in the estimation of radiation risks and probability of disease causation. NCRP Report 171, 2012.

NSRL, 2015. NSRL User Guide. Website, http://www.bnl.gov/nsrl/userguide/bragg-curves-and-peaks.php.

Norbury, J.W. and Slaba, T.C., Space radiation accelerator experiments - The role of neutrons and light ions. *Life Sci. Space Res.* **3**: 90-94, 2014.

Norman, R.B., Blattnig, S.R., De Angelis, G., Badavi, F.F., Norbury, J.W., Deterministic pion and muon transport in Earth's atmosphere. *Adv. Space Res.* **50**: 146-155, 2012.

Norman, R.B., Slaba, T.C., Blattnig, S.R., An extension of HZETRN for cosmic ray initiated electromagnetic cascades. *Adv. Space Res.* **51**: 2251-2260, 2013.

NRC, Health risks from exposure to low levels of ionizing radiation. BEIR VII Phase 2 report, 2006.

O'Neill, P.M., Badhwar-O'Neill galactic cosmic ray flux model – revised. *IEEE Trans. Nuc. Sci.*, **57**: 3148–3153, 2010.

O'Neill, P.M., Golge, S., Slaba, T.C., Badhwar-O'Neill 2014 Galactic Cosmic Ray Flux Model Description. NASA TP-2015-218569, 2015.

Simon, M.A., Cerro J.A., Latorella, K., Clowdsley, M., Watson, J., Albertson, C., Norman, R., Le Boffe, V., Walker, S., Design of two RadWorks storm shelters for solar particle event shielding. AIAA Space 2014 Conference and Exposition, 2014.

Slaba, T.C., Blattnig, S.R., Badavi, F.F., Faster and more accurate transport procedures for HZETRN. *J. Comp. Phys.* **229**: 9397-9417, 2010a.

Slaba, T.C., Blattnig, S.R., Aghara, S.K., Townsend, L.W., Handler, T., Gabriel, T.A., Pinsky, L.S., Reddell, B., Coupled neutron transport for HZETRN. *Radiat. Meas.* **45**: 173-182, 2010b.

Slaba, T.C., Qualls, G.D., Clowdsley, M.S., Blattnig, S.R., Walker, S.A., Simonsen, L.C., Utilization of CAM, CAF, MAX, and FAX for Space Radiation Analyses using HZETRN. *Adv. Space Res.* **45**: 866-883, 2010c.

Slaba, T.C., Mertens, C.J., Blattnig, S.R., Radiation shielding optimization on Mars. NASA TP 2013-217983, 2013a.

Slaba, T.C., Blattnig, S.R., Reddell, B., Bahadori, A., Norman, R.B., Badavi, F.F., Pion and electromagnetic contribution to dose: comparisons of HZETRN to Monte Carlo results and ISS data. *Adv. Space Res.* **52**: 62-78, 2013b.

Slaba, T.C. and Blattnig, S.R., GCR environmental models I: sensitivity analysis for GCR environments. *Space Weather* **12**: 217-224, 2014a.

Slaba, T.C. and Blattnig, S.R., GCR environmental models III: GCR model validation and propagated uncertainties in effective dose. *Space Weather* **12**: 233-245, 2014b.

Walker, S.A., Slaba, T.C., Clowdsley, M.S., Blattnig, S.R., Investigating material approximations in spacecraft radiation analysis. *Acta Astronautica* **69**: 6-17, 2011.

Walker, S.A., Townsend, L.W., Norbury, J.W., Heavy ion contributions to organ dose equivalent for the 1977 galactic cosmic ray spectrum. *Adv. Space Res.* **51**: 1792-1799, 2013a.

Walker, S.A., Clowdsley, M.S., Abston, H.L., Simon, M.A., Radiation exposure analysis supporting the development of solar particle event shielding technologies. 43rd International Conference on Environmental Systems, 2013b.

Wilson, J.W., Townsend, L.W., Schimmerling, W., Khandelwal, G.S., Khan, F., Nealy, J.E., Cucinotta, F.A., Simonsen, L.C., Shinn, J.L., Norbury, J.W., Transport methods and interactions for space radiations, NASA RP-1257, 1991.

Wilson, J.W., Nealy, J.E., Wood, J.S., Qualls, G.D., Atwell, W., Shinn, J.L., Simonsen, L.C., Exposure fluctuations of astronauts exposure due to orientation. NASA TP 3364, 1993.

Wilson, J.W., Miller, J., Konradi, A., Cucinotta, F.A., Shielding strategies for human space exploration. NASA CP 3360, 1997.

Wilson, J.W., Nealy, J.E., De Angelis, G., Badavi, F.F., Hugger, C.P., Cucinotta, F.A., Kim, M.Y., Dynamic/anisotropic low earth orbit environmental models. AIAA Space Conference paper 2003-6221, 2003.

Wilson, J.W., Tripathi, R.K., Mertens, C.J., Blattnig, S.R., Clowdsley, M.S., Verification and validation: High charge and energy (HZE) transport codes and future development. NASA TP-2005-213784, 2005.

Wilson, J.W., Slaba, T.C., Badavi, F.F., Reddell, B.D., Bahadori, A.A., Advances in NASA Radiation Transport Research: 3DHZETRN. *Life Sci. Space Res.* **2**: 6-22, 2014.

Wilson, J.W., Slaba, T.C., Badavi, F.F., Reddell, B.D., Bahadori, A.A., 3DHZETRN: Shielded ICRU Spherical Phantom. *Life Sci. Space Res.* **4**: 46-61, 2015.

REPORT DOCUMENTATION PAGE

Form Approved
OMB No. 0704-0188

1. REPORT DATE *(DD-MM-YYYY)*	2. REPORT TYPE	3. DATES COVERED *(From - To)*
01-03-2015	Technical Publication	

4. TITLE AND SUBTITLE

GCR Simulator Reference Field and a Spectral Approach for Laboratory Simulation

5a. CONTRACT NUMBER

5b. GRANT NUMBER

5c. PROGRAM ELEMENT NUMBER

6. AUTHOR(S)

Slaba, Tony C.; Blattnig, Steve R.; Norbury, John W.; Rusek, Adam; La Tessa, Chiara; Walker, Steven A.

5d. PROJECT NUMBER

5e. TASK NUMBER

5f. WORK UNIT NUMBER

651549.02.07.10

7. PERFORMING ORGANIZATION NAME(S) AND ADDRESS(ES)

NASA Langley Research Center
Hampton, VA 23681-2199

8. PERFORMING ORGANIZATION REPORT NUMBER

L-20550

9. SPONSORING/MONITORING AGENCY NAME(S) AND ADDRESS(ES)

National Aeronautics and Space Administration
Washington, DC 20546-0001

10. SPONSOR/MONITOR'S ACRONYM(S)

NASA

11. SPONSOR/MONITOR'S REPORT NUMBER(S)

NASA-TP-2015-218698

12. DISTRIBUTION/AVAILABILITY STATEMENT

Unclassified - Unlimited
Subject Category 93
Availability: NASA STI Program (757) 864-9658

13. SUPPLEMENTARY NOTES

14. ABSTRACT

The galactic cosmic ray (GCR) simulator at the NASA Space Radiation Laboratory (NSRL) is intended to deliver the broad spectrum of particles and energies encountered in deep space to biological targets in a controlled laboratory setting. In this work, certain aspects of simulating the GCR environment in the laboratory are discussed. Reference field specification and beam selection strategies at NSRL are the main focus, but the analysis presented herein may be modified for other facilities. First, comparisons are made between direct simulation of the external, free space GCR field and simulation of the induced tissue field behind shielding. It is found that upper energy constraints at NSRL limit the ability to simulate the external, free space field directly (i.e. shielding placed in the beam line in front of a biological target and exposed to a free space spectrum). Second, variation in the induced tissue field associated with shielding configuration and solar activity is addressed. It is found that the observed variation is likely within the uncertainty associated with representing any GCR reference field with discrete ion beams in the laboratory, given current facility constraints. A single reference field for deep space missions is subsequently identified. Third, an approach for selecting beams at NSRL to simulate the designated reference field is presented. Drawbacks of the proposed methodology are discussed and weighed against alternative simulation strategies. The neutron component and track structure characteristics of the simulated field are discussed in this context.

15. SUBJECT TERMS

Galactic cosmic ray; Radiobiology; Simulator

16. SECURITY CLASSIFICATION OF:			17. LIMITATION OF ABSTRACT	18. NUMBER OF PAGES	19a. NAME OF RESPONSIBLE PERSON
a. REPORT	b. ABSTRACT	c. THIS PAGE			STI Help Desk (email: help@sti.nasa.gov)
					19b. TELEPHONE NUMBER *(Include area code)*
U	U	U	UU	31	(443) 757-5802